

DT-MRI Based Computation of Collagen Fiber Deformation in Human Articular Cartilage: A Feasibility Study

DAVID M. PIERCE,¹ WERNER TROBIN,² JOSÉ G. RAYA,³ SIEGFRIED TRATTNIG,⁴ HORST BISCHOF,² CHRISTIAN GLASER,⁵ and GERHARD A. HOLZAPFEL^{1,6}

¹Institute of Biomechanics, Center of Biomedical Engineering, Graz University of Technology, Kronesgasse 5-I, 8010 Graz, Austria; ²Institute for Computer Graphics and Vision, Graz University of Technology, Inffeldgasse 16-II, 8010 Graz, Austria; ³Department of Clinical Radiology, Großhadern, Josef Lissner Laboratory for Biomedical Imaging, Ludwig Maximilian University of Munich, Großhadern Marchioninistrasse 15, 81377 Munich, Germany; ⁴Department of Radiology, Center of Excellence for High Field MR, Medical University of Vienna, Lazarettgasse 14, 1090 Vienna, Austria; ⁵Department of Clinical Radiology, Großhadern, Ludwig Maximilian University of Munich, Großhadern Marchioninistrasse 15, 81377 Munich, Germany; and ⁶Department of Solid Mechanics, School of Engineering Sciences, Royal Institute of Technology (KTH), Osquars Backe 1, 100 44 Stockholm, Sweden

(Received 16 November 2009; accepted 25 February 2010; published online 12 March 2010)

Associate Editor Michael S. Detamore oversaw the review of this article.

Abstract—Accurate techniques for simulating the deformation of soft biological tissues are an increasingly valuable tool in many areas of biomechanical analysis and medical image computing. To model the complex morphology and response of articular cartilage, a hyperviscoelastic (dispersed) fiber-reinforced constitutive model is employed to complete two specimen-specific finite element (FE) simulations of an indentation experiment, with and without considering fiber dispersion. Ultra-high field Diffusion Tensor Magnetic Resonance Imaging (17.6 T DT-MRI) is performed on a specimen of human articular cartilage before and after indentation to ~20% compression. Based on this DT-MRI data, we detail a novel FE approach to determine the geometry (edge detection from first eigenvalue), the meshing (semi-automated smoothing of DTI measurement voxels), and the fiber structural input (estimated principal fiber direction and dispersion). The global and fiber fabric deformations of both the un-dispersed and dispersed fiber models provide a satisfactory match to that estimated experimentally. In both simulations, the fiber fabric in the superficial and middle zones becomes more aligned with the articular surface, although the dispersed model appears more consistent with the literature. In the future, a multi-disciplinary combination of DT-MRI and numerical simulation will allow the functional state of articular cartilage to be determined *in vivo*.

Keywords—Finite element simulation, Constitutive modeling, Hyperviscoelasticity, Magnetic resonance imaging, Diffusion tensor.

Address correspondence to Gerhard A. Holzapfel, Institute of Biomechanics, Center of Biomedical Engineering, Graz University of Technology, Kronesgasse 5-I, 8010 Graz, Austria. Electronic mail: holzapfel@tugraz.at

INTRODUCTION

In a typical diarthrodial joint, such as the human knee joint, the opposing bones are covered with a layer of dense connective tissue, the articular cartilage, which provides the articulating surfaces. Within the cartilage (composed of fluid, electrolytes, chondrocytes, collagen fibers, proteoglycans and other glycoproteins, cf. Mow *et al.*⁴⁷) fibers of predominantly Type II collagen provide tensile strength and stiffness to the solid phase, a proteoglycan gel. The collagen fibers exhibit a high level of structural organization usually consisting of three sub-tissue zones starting from the surface to the subchondral bone: the superficial tangent zone has fibers which are predominantly tangential to the articular surface, the middle zone has fibers which are isotropically distributed and oriented, and the deep zone has fibers which are oriented predominantly perpendicular to the bone.

Given the complex layered structural organization of Type II collagen fibers, and the importance of this collagen fiber fabric in the mechanical properties of articular cartilage, many destructive and nondestructive experimental methods have been pursued to characterize the fiber orientation and density. Destructive methods to accomplish this goal rely on histological sectioning (possibly with staining) and include scanning electron microscopy (SEM),^{13,24,31,35–37} Fourier transform infrared (FT-IR) imaging and microspectroscopy⁸ and Polarized Light Microscopy (PLM),^{9,16} the current standard for measuring average fiber

orientation. There is also considerable interest in determining the structural arrangement of collagen fibers nondestructively. Methods to accomplish this include differential interference contrast light microscopy,¹⁰ Small Angle X-ray Scattering (SAXS),^{45,46,48} Optical Coherence Tomography (OCT) and polarization sensitive optical coherence tomography (PS-OCT),^{61,62} spin-spin relaxation time T2-weighted Magnetic Resonance Imaging (T2w MRI)^{16,71} and high field Diffusion Tensor MRI (DT-MRI).^{16,17,20,44}

MRI is certainly the most advanced and widely used *in vivo* imaging technique for cartilage. Recent techniques such as delayed Gadolinium-Enhanced MRI of Cartilage (dGEMRIC) or T2-relaxation time quantification show a high potential for *in vivo* compositional and gross structural analysis of the cartilage matrix. However, they do not provide direct directional information on the collagenous fiber architecture available from DT-MRI studies.^{16,17,20,44}

Accurate techniques for simulating soft tissue deformation are an increasingly valuable tool in many areas of medical image computing, as noted by Taylor *et al.*⁶⁰ Finite element (FE) simulation is a well-accepted means by which to gain insight on the functional relationships between structure and mechanical properties within articular cartilage. Several constitutive models for cartilage have been proposed. An early two-phase constitutive model employed a linear biphasic poroviscoelastic approach with two relaxation time constants.¹⁸ A fibril reinforced poroelastic model employing viscoelastic springs in a simplified 2D axisymmetric geometry was later proposed.⁴⁰ Three-phase models include a poroviscoelastic 2D axisymmetric approach with idealized viscoelastic fiber reinforcement (Benninghoff-type architecture⁶), which also include swelling effects due to the fixed-charge densities of the proteoglycans.^{65,66} This model can explain the depth dependent compressive properties of cartilage by varying the material composition along the depth, not the intrinsic properties of the constituents.⁶⁴ A recent constitutive model combines a biphasic viscohyperelastic matrix with viscous fibers, again employing 2D axisymmetry with a simplified fiber geometry.²¹

Recently, attempts have also been made to incorporate imaging data into such constitutive models for cartilage. Depth-dependent collagen data quantified by polarized light microscopy was included in a 2D axisymmetric fibril-reinforced FE analysis with an idealized geometrical collagen structure.³² The approach was extended to include depth-dependent collagen content and fibril orientation as well as proteoglycan and water content derived from experiment.^{33,63} Additionally, a means to model collagen network contributions to the cartilage response has been introduced, attempting to bridge the gap between

experimental data on the collagen structure and theoretical tools for simulating cartilage, but the formulation was not implemented in a full 3D FE simulation.⁵³

In this study, ultra-high field DT-MRI (17.6 T) is used to inform, and hence add fidelity to, a specimen-specific finite element simulation of an indentation experiment (for which pre- and post-indentation DT data are generated). Articular cartilage is recognized as a multi-phase material; however, some simplifying assumptions facilitate the current constitutive model and related simulation. By considering only two main components: (i) a homogenous proteoglycan/water gel matrix material (proteoglycans, other proteins, chondrocytes plus water and electrolytes) and (ii) a collagen fiber fabric or collagenous fiber network (anisotropic entanglement of Type II collagen fibers), articular cartilage may be considered a time-dependent (dispersed) fiber reinforced material,^{12,18,20} an extension of the material model detailed in Pierce *et al.*⁵¹

In light of the complexity of cartilage constitutive modeling, the motivation of our study is as follows: (i) provide an engineering basis to quantitatively relate the material properties and mechanical response of articular cartilage to the underlying mechanical structure, (ii) enable large deformation, inhomogeneous, anisotropic, time-dependent simulations of full joint deformation, (iii) relate the simulation results to MRI data from a specific specimen, (iv) enable further studies of articular cartilage degeneration in a multi-disciplinary setting that includes computational mechanics.

METHODS

To model articular cartilage we employ a viscoelastic finite strain model considering the dispersed collagen fiber orientations. An indentation experiment, for which pre- and post-indentation data are generated, is completed using ultra-high field DT-MRI (17.6 T). The specimen geometry and an element-wise map of the collagen fiber structure (principal directions and dispersion) is estimated directly from the DT-MRI data and distilled into a suitable FE mesh. Simulations are completed with and without the inclusion of fiber dispersion and compared directly against the experimentally determined deformation (both global and fiber fabric). Here we detail the constitutive model, the DT-MRI experiment, the FE simulation and, finally, the implementation of collagen fiber DTI data in the FE simulation.

Constitutive Model

To model the complex cartilage morphology and material response, a viscoelastic finite strain model

considering the dispersed collagen fiber orientations is employed, with various constituents documented in Holzapfel *et al.*,²⁷ Gasser *et al.*²² and Pierce *et al.*⁵¹ Brief justification for the modeling assumptions is provided later, as well as an overview of the mathematical model and parameters.

In the formulation employed, the matrix material and the collagen fabric are modeled as independent viscoelastic materials. Viscoelasticity of the matrix material is included to capture both the intrinsic time-dependent properties of the solid phase (proteoglycan matrix without collagen fiber reinforcement) and its interaction with the interstitial fluid.^{4,18,21,68} Many studies also provide justification for including time dependence in the collagenous fiber network. A viscoelastic response from cartilage has been observed experimentally in tensile testing (in which the fluid pressure is negligible and the contribution from the proteoglycan matrix is likely low), thus the collagen fibers must play a dominant role in the observed viscoelasticity.^{40,54–56} Furthermore, the viscoelastic shear modulus of cartilage has been reported to increase with collagen cross-links, which further indicates that the collagen fibers are viscoelastic.^{25,72}

Experimentally determined values of Poisson's ratio for cartilage material show significant variability in the literature, varying from 0 to 2.1 depending on the loading condition and experimental techniques employed.^{12,47} Several authors have proposed that cartilage tissue behaves nearly isochorically under physiological levels of pressures (in the range of 2–12 MPa⁵⁰) and loading durations (< 10 s).^{4,30,34,68} This behavior is due to the low permeability of the cartilage solid matrix and the intrinsic incompressibility of the constituents. Thus, under most loading configurations the total tissue volume will not change for tens of seconds even at loading rates as low as 0.25 $\mu\text{m/s}$.

To reproduce the mechanical indentation data, and hence study the fiber fabric deformation response, we employed an isochoric material model. Due to the isochoric aspect of the model, the full deformation state determined by the constitutive volumetric response will provide good approximations to the true material response during loading and initial relaxation, but lateral deformations will stray from the physical response during prolonged relaxation to thermodynamical equilibrium (which includes loss of fluid).

We use a convex strain-energy function Ψ to specify a nonlinear material undergoing finite strains. A multiplicative split of the deformation gradient \mathbf{F} into volumetric and isochoric contributions is employed, using the isochoric deformation gradient $\bar{\mathbf{F}} = J^{-1/3}\mathbf{F}$, where $J = \det \mathbf{F}$ is the Jacobian, and, similarly, the modified right Cauchy–Green tensor $\bar{\mathbf{C}} = J^{-2/3}\mathbf{C}$, where $\mathbf{C} = \mathbf{F}^T\mathbf{F}$.²⁶ We assume the decoupled form

$\Psi = U(J) + \bar{\Psi}$, where the volumetric contribution is particularized as $U(J) = K(J - 1)^2/2$; here K is a stress-like material parameter, which in the case of isochoric deformation degenerates to a non-physical, (positive) penalty parameter used to enforce incompressibility.

Next, $\bar{\Psi}$ is chosen to include matrix $\bar{\Psi}_m$ and fiber $\bar{\Psi}_f$ contributions independently such that

$$\bar{\Psi}(\bar{\mathbf{C}}, \mathbf{a}_0) = \bar{\Psi}_m(\bar{\mathbf{C}}) + \bar{\Psi}_f(\bar{\mathbf{C}}, \mathbf{a}_0), \quad (1)$$

where the principal direction of the collagen fibers is characterized by the (reference) direction vector \mathbf{a}_0 , with $|\mathbf{a}_0| = 1$. For simplicity, $\bar{\Psi}$ is particularized to include only \bar{I}_1 and \bar{I}_4 .²⁸ Thus,

$$\bar{\Psi}(\bar{I}_1, \bar{I}_4) = \bar{\Psi}_m(\bar{I}_1) + \bar{\Psi}_f(\bar{I}_1, \bar{I}_4), \quad (2)$$

where $\bar{I}_1 = \text{tr} \bar{\mathbf{C}}$ and $\bar{I}_4 = \bar{\mathbf{C}}:\mathbf{a}_0 \otimes \mathbf{a}_0$ such that anisotropy arises only through the (modified) invariant \bar{I}_4 . Note that \bar{I}_4 has a clear physical interpretation as it is the square of the stretch of the collagen fiber fabric in the direction \mathbf{a}_0 .

Finally, the matrix $\bar{\Psi}_m$ and fiber $\bar{\Psi}_f$ contributions to the function $\bar{\Psi}$ must be particularized in a manner capable of reproducing the experimentally observed cartilage response.

Isotropic Matrix Material

Bachrach *et al.*⁴ argue that anisotropy arises primarily from the collagen fiber fabric so that the remaining matrix material is best treated as isotropic. Furthermore, for the low loading domain the (wavy) collagen fibers of soft collagenous tissues are not active (they do not store strain energy). For the purposes of this study, the neo-Hookean model was chosen to capture the matrix material, and hence $\bar{\Psi}_m$ is specified as

$$\bar{\Psi}_m(\bar{I}_1) = \frac{\mu}{2}(\bar{I}_1 - 3), \quad (3)$$

where $\mu > 0$ is a stress-like material parameter, corresponding to the shear modulus of the underlying matrix material in the reference configuration.

Anisotropic Fiber Fabric

The anisotropic, nonlinear response of the dispersed collagen fiber fabric is captured phenomenologically by a strain-energy function extended to consider the dispersion of the collagen fiber orientation as

$$\begin{aligned} \bar{\Psi}_f(\bar{I}_1, \bar{I}_4) &= \frac{k_1}{2k_2} \left\{ \exp[k_2(\bar{I}_4^* - 1)^2] - 1 \right\}, \\ \bar{I}_4^* &= \kappa \bar{I}_1 + (1 - 3\kappa)\bar{I}_4, \end{aligned} \quad (4)$$

where κ is an additional scalar structure parameter characterizing the dispersion of the collagen fiber

fabric about the direction \mathbf{a}_0 (which extends the model employed previously⁵¹) according to Gasser *et al.*,²² $k_1 > 0$ is a stress-like material parameter and $k_2 > 0$ is a dimensionless material parameter, which altogether control the nonlinear, equilibrium fiber fabric response. The form of this strain-energy function is based on the experimentally supported assumption that the collagen fiber fabric has a strong nonlinear stiffening response under tension.²⁸

In Eq. (4) the right Cauchy-Green-like quantity \bar{I}_4^* is introduced. It is a deformation measure in the direction of the mean orientation \mathbf{a}_0 of the collagen fiber fabric. Since collagen fibers cannot support compression a tension/compression nonlinearity stems from the conditional statement that the anisotropic part $(1 - 3\kappa)\bar{I}_4$ contributes to $\bar{\Psi}_f$ only if the deformation in the direction of \mathbf{a}_0 is positive, i.e. $\bar{I}_4 > 1$, the collagen fibers only engage under stretches greater than unity.²²

This extension of the modified fourth invariant is able to represent dispersion of the fiber orientation through the additional dispersion (structure) parameter $\kappa \in [0, 1/3]$. For $\kappa = 0$ the expression $\bar{I}_4^* = \bar{I}_4$ is returned representing the model according to Pierce *et al.*⁵¹ In that case the assumption $\bar{I}_4 > 1$ is also sufficient for convexity of $\bar{\Psi}_f$.²⁹ For $\kappa = 1/3$ the expression $\bar{I}_4^* = \bar{I}_1/3$ is achieved. It corresponds to an isotropic distribution, similar to that of Demiray.¹⁴ Thus, the model can represent a range of collagen fiber distributions between perfect fiber alignment ($\kappa = 0$) and perfect isotropy ($\kappa = 1/3$). It is also assumed that the fiber family is distributed with rotational symmetry about the mean referential direction \mathbf{a}_0 so that the distributed fibers contribute a transversely isotropic character to the overall response of the material.

Hence, the parameter κ , representing the fiber dispersion, describes the ‘degree of anisotropy’. A methodology to locally identify both \mathbf{a}_0 and κ directly from the available DTI data is detailed in the section “[Model Implementation of Collagen Fiber DTI Data](#)”.

Determination of Stresses and Algorithmic Stress Tensor

To illustrate the material model based on the strain-energy functions, we elaborate the relationship between the (input) deformation gradient \mathbf{F} and the Cauchy stress tensor $\boldsymbol{\sigma} = J^{-1}\mathbf{F}\mathbf{S}\mathbf{F}^T$, where \mathbf{S} is the second Piola-Kirchhoff stress tensor, which is specified by summing the volumetric, matrix, fiber fabric and viscoelastic contributions. Thus,

$$\mathbf{S} = \mathbf{S}_{\text{vol}} + \sum_{\alpha=\text{m,f}} (\mathbf{S}_\alpha + \mathbf{Q}_\alpha), \quad (5)$$

where $\mathbf{S}_{\text{vol}} = 2\partial U(J)/\partial \mathbf{C}$ is the volumetric, $\mathbf{S}_m = 2\partial \bar{\Psi}_m/\partial \mathbf{C}$ is the matrix, and $\mathbf{S}_f = 2\partial \bar{\Psi}_f/\partial \mathbf{C}$ is the fiber

fabric contribution to the second Piola-Kirchhoff stress tensor \mathbf{S} , respectively, and \mathbf{Q}_α represent the viscoelastic contributions where $\alpha = \{\text{m}, \text{f}\}$ time-dependent processes are employed.

Next, to determine the time-dependent (viscous) response of the matrix material and the fiber fabric, assume that at times t_n and t_{n+1} all relevant kinematic quantities are given. In addition to that, the stress \mathbf{S}_n at time t_n is also specified uniquely via the associated constitutive equation serving as an ‘initial’ data base. All that remains is the computation of the second Piola-Kirchhoff stress tensor \mathbf{S}_{n+1} at time t_{n+1} (the algorithmic stress tensor generalized from Eq. 5), which is given in the form

$$\mathbf{S}_{n+1} = \left[\mathbf{S}_{\text{vol}} + \sum_{\alpha=\text{m,f}} (\mathbf{S}_\alpha + \mathbf{Q}_\alpha) \right]_{n+1}. \quad (6)$$

The stress contributions $\mathbf{S}_{\text{vol},n+1}$, $\mathbf{S}_{m,n+1}$ and $\mathbf{S}_{f,n+1}$ describe the total elastic response and can be computed from the given strain measures at t_{n+1} . The term $\mathbf{Q}_{\alpha,n+1}$ in Eq. (6) represents the non-equilibrium stresses at time t_{n+1} and is responsible for the viscoelastic stress contribution (controlled by parameters: β_α , a dimensionless strain-energy factor controlling the magnitude of the viscous component response, and τ_α , the associated relaxation time). This is evaluated using the *mid-point rule* to arrive at a second-order accurate *recurrence update formula* for the non-equilibrium stresses, determined from the known stresses \mathbf{Q}_α and \mathbf{S}_α at t_n (for numerical purposes we have assumed $\mathbf{Q}_\alpha^{0+} = \mathbf{O}$), see Simo.⁵⁷ At thermodynamical equilibrium $\mathbf{Q}_\alpha = \mathbf{O}$ as well, which means that only the elastic response remains, i.e. the response controlled by the material parameters μ , k_1 , k_2 and the structure parameters \mathbf{a}_0 and κ . In the DTI experiment only two configurations of the collagen fiber fabric are known: the undeformed configuration and the equilibrium deformed configuration. Hence, only the elastic (time-independent) contribution to the global deformation and stress response is considered in the current work.

In summary, for the current work only the three material parameters and two structure parameters controlling the elastic (time independent) response are required to determine the equilibrium deformation (Table 1). The material parameter values are based on the mean response of 23 individual indentation experiments performed on 5 specimens of human articular cartilage,⁵¹ while the structure parameters are extracted directly from the DT-MRI data.

This extended constitutive model was implemented in the FE analysis program FEAP.⁵⁹

TABLE 1. Parameter set used for the time independent simulation of deformation response in human articular cartilage: material parameters μ , k_1 and k_2 from Pierce *et al.*⁵¹ and structure parameters a_0 and κ determined from the DT-MRI data on an element-wise basis (henceforth, including fiber dispersion means $\kappa \in [0, 1/3]$).

μ (MPa)	k_1 (MPa)	k_2	a_0	κ
0.417	0.425	39.8	111	[0, 1/3]

MRI Experiment

Diffusion Tensor Imaging (DTI or DT-MRI) is a magnetic resonance imaging (MRI) technique which allows the microstructure of soft biological tissues to be probed by determining the mobility of water molecules, i.e. the diffusivity characteristics. In articular cartilage, these diffusional properties are essentially controlled by two components: (i) a homogenous ground substance of a proteoglycan–water gel that gives a baseline isotropic diffusivity and (ii) a highly anisotropic collagenous fiber network that overlays the baseline.²⁰ Recent publications have reported that the anisotropic diffusion of water in cartilage, as visualized by DT-MRI, reflects the general orientation of the (largely Type II) collagen fibers.^{1,15–17,20,44,52} In fact, DT-MRI yields specific and precise information about the *local* morphological structure of articular cartilage at micron length scales. For further details about DT-MRI techniques and their widespread clinical applications, see, e.g. Le Bihan *et al.*³⁹ and references therein.

In this study, ultra-high field DT-MRI (17.6 T) is used to capture data on indentation experiments performed on a specimen of human articular cartilage. The data, in turn, are used to inform a corresponding specimen-specific FE simulation of the indentation experiment. Herein, we start with a brief introduction to diffusion tensor imaging and then describe the indentation experiment, the specific DT-MR imaging, and the resulting data acquired before and after compression.

Indentation Experiment

In the present study, the left patella of a healthy 27-year-old male donor is harvested within 24 h from death, rinsed with physiologic solution and stored for 36 h at 4 °C until the MRI experiment began. Just before MRI examination a cylindrical cartilage-on-bone specimen of 7 mm diameter is drilled from the central part of the lateral facet of the patellar cartilage. Using a scalpel, the specimen is then cut into a cuboid form to fit into a glass vessel of 4 mm internal diameter, which fitted tightly into a 5 mm birdcage coil used for the MRI experiments. The cuboid has a footprint

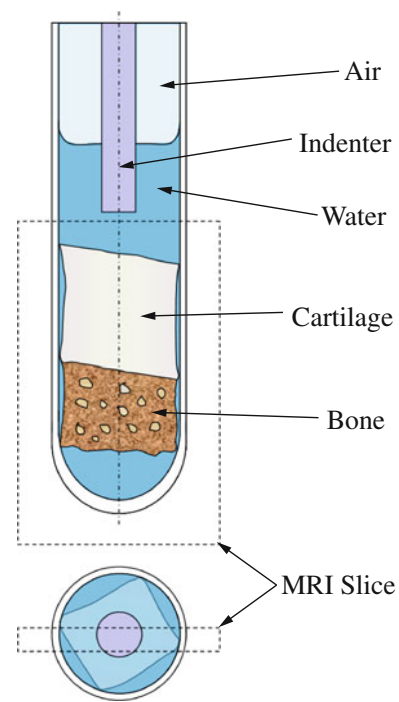


FIGURE 1. Schematic representation of the setup and specimen position for the MRI experiments. A cuboid shaped cartilage-on-bone specimen is placed in a cylindrical glass vessel partially filled with physiologic solution (indicated as water). The cartilage specimen is pushed to the bottom of the vessel so that its corners tightly fit the inner walls of the vessel. A cylindrical indenter of 1.5 mm diameter is used for the indentation experiment. The slice position for MRI is indicated by the dashed outline in both views.

slightly larger than 2.8 mm square ($\sim 2.8 \text{ mm} \times 2.8 \text{ mm} \times 2.6 \text{ mm}$ for the cartilage layer, with the bone another $\sim 1 \text{ mm}$ in thickness) to ensure that the corners of the cuboid specimen touch the walls of the glass vessel, such that the specimen remains fixed within the vessel.

The specimen is then placed within the vessel under physiologic solution to avoid the formation of air bubbles in the specimen, which can lead to susceptibility artifacts (Fig. 1). During the MRI experiment, the specimen remains immersed in physiologic solution to avoid drying, and the temperature is maintained at 17–19 °C using a gradient cooling system.

MRI measurements are first performed on the unindented specimen. The slice position (one measurement slice is acquired) for all MRI experiments is oriented diagonally within the cuboid to maximize the imaged cartilage volume (again, Fig. 1).

After all measurements are completed on the unindented configuration, the specimen is taken out of the scanner and indented $\sim 0.50 \text{ mm}$ (resulting in a compression of $\sim 20\%$) using a cylindrical, flat-tipped glass indenter with a 1.5 mm diameter. The specimen is allowed to reach thermodynamic equilibrium

(20 min rest) before measuring it again using the same MRI protocol. Since the specimen must be removed from the scanner to perform indentations, the images between acquisitions may be slightly displaced.

MRI Protocol

The MRI experiments are performed with a 17.6 T scanner (UltraStabilized magnet system, Bruker Bio-Spin, Rheinstetten, Germany) using a one channel 5 mm birdcage coil provided by the manufacturer. DTI is performed with a diffusion-weighted spin echo sequence (TR = 937.5 ms, TE = 13 ms, Image matrix = 256×128 , squared field of view = 12.8 mm, slice thickness = $800 \mu\text{m}$, image resolution = $50 \times 100 \mu\text{m}$, number of averages = 10, total acquisition time = 20 min). Acquisition time is optimized to guarantee a signal-to-noise-ratio (SNR) larger than 10 near the bone–cartilage interface. Images are acquired with a b -value of 0 s/mm^2 and with a b -value of 550 s/mm^2 in six different directions (which minimizes the measurement error using the Crámer-Rao-lower bound approach, total acquisition time of the DTI experiment $\sim 2 \text{ h } 20 \text{ min}$). (Note on SNR: MRI measurements in the deep cartilage zones are difficult because of the low water content and the low T2 values, i.e. a very low signal is present. However, there is always a very strong SNR for the rest of the cartilage volume. For example, typical SNR values in the middle zone are on the order of 300. SNR is calculated from the $b = 0 \text{ s/mm}^2$ images, so that they are affected only by T2-weighting, which is the same in all DTI images due to the constant TE.)

To avoid artifacts caused by long-term eddy currents associated with the diffusion gradients, half of the averages are acquired with diffusion gradients of the same polarization and the remaining half are acquired with diffusion gradients of with the opposite polarization.⁷ The geometric mean of the images acquired in this manner results in images free from long-term eddy current artifacts.⁴⁹ The b -matrix is calculated from the pulse sequence considering all gradients in the sequence in order to improve accuracy in the diffusion tensor calculation.⁴³

Available MRI Data

In order to motivate the subsequent use in FE modeling, the diffusion tensor field acquired by the measurement process outlined above is discussed briefly. Once the diffusion tensor is calculated, its eigenvectors and eigenvalues are calculated. Let \mathbf{A} be one such tensor, where the unique solution to the eigenproblem $\mathbf{A}\hat{\mathbf{n}}_i = \Lambda_i\hat{\mathbf{n}}_i$, $i = 1, 2, 3$; no summation, leads to the eigenbasis $\hat{\mathbf{n}}_i$, with corresponding eigenvalues Λ_i . Figures 2a and 2b depict the first principal

eigenvalues of the tensor field in the undeformed and fully deformed configurations, respectively. In Fig. 2a, the rectangular gray area is the articular cartilage layer and the noisy black area directly below is the subchondral bone. The cartilage–bone specimen is surrounded by water (solid white, representing a higher diffusivity) and is enclosed in a cylindrical container (solid black border). In Fig. 2b, the glass indenter (noisy black rectangle, top-center) and its effect on the cartilage layer are observed.

Mechanical preparation of the cartilage specimen led to a small fissure close to the cartilage–bone transition (indicated in Fig. 2a). Since this fissure is quite far from the indentation location it is homogenized in the modeling (meshing) process to avoid numerical problems.

For further analysis, the mean diffusivity (ADC, $\bar{\Lambda} = 1/3\text{tr}\mathbf{A}$) and the fractional anisotropy (FA),

$$\text{FA} = \sqrt{\frac{2}{3} \frac{(\Lambda_1 - \bar{\Lambda})^2 + (\Lambda_2 - \bar{\Lambda})^2 + (\Lambda_3 - \bar{\Lambda})^2}{\Lambda_1^2 + \Lambda_2^2 + \Lambda_3^2}}, \quad (7)$$

are calculated for each voxel. The resulting pre-indentation (undeformed configuration) DTI data is shown in Fig. 3, to further demonstrate the richness of the available data. Figures 3a and 3b are close-up views of the specimen, where the FA is visualized as a heat map, illustrating the degree of anisotropy in each measurement voxel.^{19,20,44} For the sake of visual clarity and increased contrast, the fractional anisotropy is clamped to the ranges $[0, 0.15]$ and $[0, 0.30]$, depicted in Figs. 3a and 3b, respectively.

As labeled in Fig. 3, the three cartilage layer zones can be identified, as well as the underlying bone. The

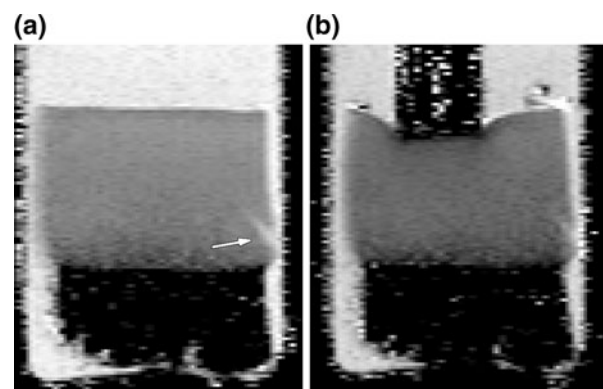


FIGURE 2. Grayscale representation of the first principal eigenvalues of the DT-MRI data in (a) pre-indentation, and (b) post-indentation configurations. Principal diffusion in water is represented using white voxels, while regions with negligible water content are represented as black voxels (i.e. glass). Intermediate values span the range from black to white. Note a small fissure close to the cartilage–bone transition indicated by the white arrow.

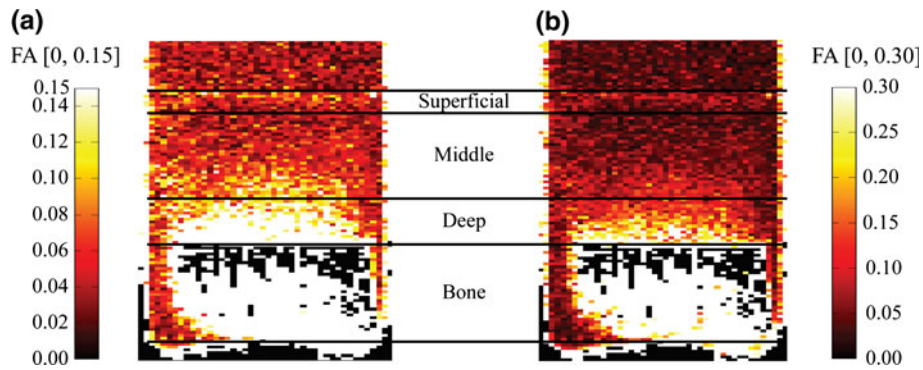


FIGURE 3. Visualization of the DTI data in the undeformed configuration for two ranges of fractional anisotropy: (a) FA [0, 0.15], and (b) FA [0, 0.30]. The three cartilage layer zones can be identified, as well as the underlying bone.

relative thickness of each zone in the specimen is determined directly from the DTI data to be 15, 55, and 30% for the superficial tangent, middle, and deep zones, respectively. Furthermore, the images also show that the anisotropy is lowest in the middle zone. These values and observations are consistent with the literature (cf. Mow *et al.*⁴⁷). Such data are available in both the pre- (as shown) and post-indentation configurations.

Finite Element Simulation

Informed by the ultra-high field DT-MRI, finite deformation contact simulations of the indentation experiment are completed using two constitutive models (without and with fiber dispersion). Details of the FEA geometry and mesh, the implementation of DTI data on the collagen fiber structure and the indentation simulation are provided here.

FEA Geometry and Mesh

In order to model the experiment, the geometry of the cartilage, as well as the initial/final location and orientation of the indenter are estimated from the DT-MRI data. The first step toward a specimen-specific geometry is to extract outer boundaries of the cartilage region from both sets of MRI data, i.e. in the undeformed and deformed configurations (since we will later compare the simulation results to the experimentally measured deformation). The principal eigenvalues of the reconstructed tensors (see Figs. 2 and 3) reveals a ‘partial volume effect’ at the specimen edges, i.e. there are no sharp edges. Every voxel is assigned the average diffusivity of the volume it encompasses. Hence, the diffusivity measured for voxels along the (averaged) cartilage/water boundary is higher than for voxels inside the cartilage.

Manually specified boundaries are refined using an automatic edge-detection method to ensure reproducible

results. This automatic edge refinement achieves sub-voxel accuracy, which avoids constraining the boundaries to the rough voxel grid, and consistently accounts for the partial volume effect. We place a 1D search window (nine voxels wide) orthogonal to the manually specified boundary and define the sub-voxel-accurate zero-crossing of the second derivative as the edge location. To limit the influence of image noise, the differentiation is performed on a smoothed version of the input image. The combination of these two linear filters (Gaussian smoothing followed by a discrete Laplacian) is widely known as the Laplacian of Gaussian (LoG) filter or the Marr-Hildreth-Operator.⁴²

Larger smoothing factors (σ , voxels or mm) naturally lead to smoother boundaries, but the edge location may change with increasing σ —a well-known result from scale space theory.⁶⁷ The σ value should, therefore, be chosen as low as possible to eliminate the ‘shifting’ effect, and simultaneously high enough to avoid interferences due to measurement noise. In the current work, $\sigma = 2.0$ is chosen to generate the known specimen width, which yields smooth and reproducible results.

Figures 4a–4c demonstrate how the available MR Images are used to generate a 3D specimen-specific FE model. Figure 4a shows the first principal eigenvalue map with the 2D specimen outline generated using the LoG filter ($\sigma = 2.0$), cf. Fig. 2a; the FE coordinate system is also indicated.

Next, the subpixel accurate polygon of the cartilage boundary must be discretized in 2D. To facilitate a direct mapping from the DTI data the voxel grid from the DTI measurement is used as a structured FE mesh. Naturally, this mapping breaks down near the cartilage borders. Figure 4b shows the resulting outer boundary with the unmodified DT-MRI voxel grid. A semi-automatic process is used to generate a 2D mesh of elements with good aspect ratios starting from the

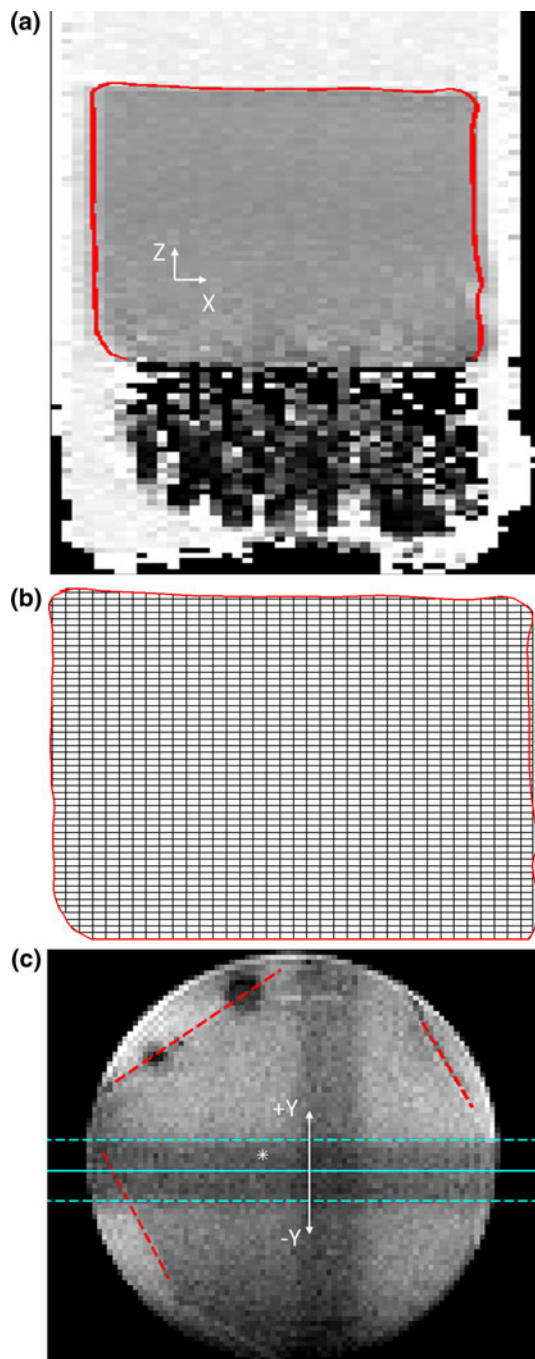


FIGURE 4. (a) Grayscale representation of the first principal eigenvalue map shown with the 2D specimen outline generated using the LoG filter with $\sigma = 2.0$, cf. Fig. 2(a), (b) the resulting specimen boundary with the unmodified DT-MRI voxel grid, (c) axial view of the specimen (grayscale representation of the first principal eigenvalue map in the undeformed configuration); the location of the DTI measurement slice, the estimated specimen boundaries and the indenter center are all indicated. In the grayscale images, principal diffusion in water is represented using white voxels, while regions with negligible water content are represented as black voxels. Intermediate values span the range from black to white.

voxel grid and the cartilage boundary, a subpixel accurate polygon.

The refined 2D elements must next be extruded to a volume and discretized to generate 3D finite elements. The corrected 2D quadrilateral mesh is extruded normal to the DTI measurement plane along the specimen boundaries estimated from an additional axial view as shown in Fig. 4c. In this axial view of the undeformed specimen the location of the DTI measurement slice, the estimated specimen boundaries, and the indenter center are all indicated. Thus, the available cross-sections can be used to estimate the 3D specimen-specific geometry.

For numerical reasons the extrusion is not extended to the specimen extremes in the $\pm y$ directions (both run time minimization and element shape preservation). Truncating the extrusion before the specimen extremes does not effect the solution in the DTI slice region (the region of interest). The final simulations employ 25,194 eight-node brick elements based on a mixed Jacobian-pressure formulation (a three-field variational principle, see Simo *et al.*⁵⁸). The resulting undeformed cartilage mesh, cylindrical containment vessel and aligned indenter are shown in Fig. 5.

Model Implementation of Collagen Fiber DTI Data

Once the FE geometry and mesh are finalized, an element-wise map of the fiber fabric (\mathbf{a}_0 and κ) is estimated for the through-thickness zones directly from the DTI data. Here we describe a process for distilling the local tensor-valued data into the FE mesh to add fidelity to the FE simulation. By construction, one tensor per element is available for extraction within ‘inner’ regions of the mesh, i.e. there is a one-to-one mapping from tensors to elements. Due to geometrical constraints on the FE mesh, this one-to-one mapping breaks down along the boundary. Furthermore, the extruded elements are slightly shifted and distorted compared to the reference slice, which also invalidates any direct mapping. As such, a physically meaningful interpolation of the tensorial information is required.

The following setup is employed: first the element centroids are calculated and projected back to the DTI slice along the extrusion direction (the y axis). Since the projected elements are at most as large as a DTI voxel, we simply assign the four nearest neighbors in the DTI data to every centroid and compute weights inversely proportional to their respective distances. Finally, these four tensors are interpolated in the Log-Euclidean framework presented by Arsigny *et al.*³ (Their Log-Euclidean mean is a generalization of a geometric mean to the space of symmetric positive-definite matrices.)

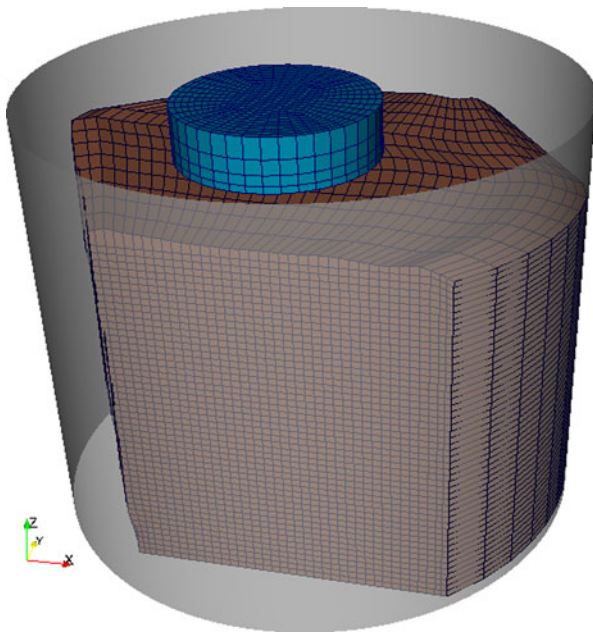


FIGURE 5. Final undeformed cartilage mesh, cylindrical containment vessel and aligned indenter.

At this point, one tensor of diffusion data is estimated per finite element. Let \mathbf{A} be one such DTI data tensor for a specific finite element in the mesh, where the unique solution to the eigenproblem leads to the eigenbasis $\hat{\mathbf{n}}_i$, with corresponding eigenvalues Λ_i . The eigenvector corresponding to the first principal eigenvalue is taken as the principal direction of anisotropy resulting from the collagen fiber fabric, i.e. $\mathbf{a}_0 = \hat{\mathbf{n}}_1$. Figure 6 demonstrates the resulting principal directions of the collagen fibers in the superficial, middle and deep zones. These orientations are consistent with physiological distributions recorded in the literature (cf. Mow *et al.*⁴⁷).

Given the principal direction \mathbf{a}_0 for a specific element, the corresponding structure parameter κ can be estimated using an adjusted set of ‘eigenvalues’ determined by a normalization condition, i.e.

$$\alpha_i = \frac{\Lambda_i}{\text{tr}\mathbf{A}} = \frac{\Lambda_i}{\Lambda_1 + \Lambda_2 + \Lambda_3}; \quad i = 1, 2, 3, \quad (8)$$

such that the normalized values meet the required restriction $\alpha_1 + \alpha_2 + \alpha_3 = 1$. Next, transverse isotropy, as required by the constitutive model, is ensured (by a transversely isotropic condition) as $\alpha_{2T} = \alpha_{3T} = (\alpha_2 + \alpha_3)/2$. This mapping to the adjusted ‘eigenvalues’ $\alpha_1, \alpha_{2T}, \alpha_{3T}$ fulfills all normalization requirements of the model as discussed in Gasser *et al.*²² and captures a physically meaningful measure of the fiber dispersion. As a result, κ is directly available as $\kappa = \alpha_{2T} = \alpha_{3T}$. The transversely isotropic condition used in the mapping of κ does not pose any problems

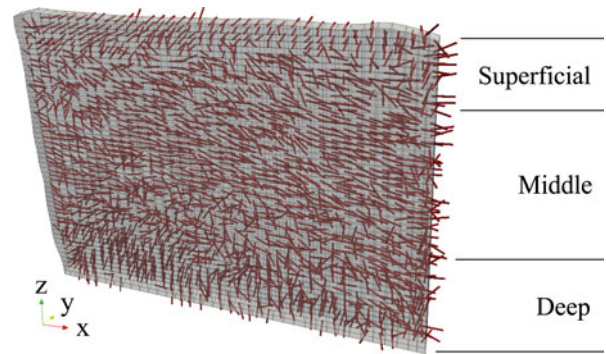


FIGURE 6. A single-element thickness FE mesh representation of the layered structural arrangement of Type II collagen fibers within the specific articular cartilage specimen used in this study, as determined directly from DTI data (voxel resolution $50 \times 100 \times 800 \mu\text{m}$, cf. Fig. 3).

in light of the original data, as the data do not contain any tensors with a pronounced ‘plate-like’ shape. Oblate, or ‘plate-like’ tensors occur when the first and second eigenvalues of the tensor are significantly larger than the third eigenvalue. This does not occur within the articular cartilage volume; the ratio Λ_2/Λ_3 is near unity (min: 1.0008, max: 2.3348—due to measurement noise near the cartilage-bone transition, mean: 1.1265, and 95th percentile: 1.4524).

The resulting fiber dispersion can be seen in Fig. 7, which illustrates the layer-specific dispersion of the structure parameter κ in the three cartilage zones: Fig. 7a superficial tangential, Fig. 7b middle, and Fig. 7c deep.

Indentation Simulation

To complete the FE simulation the boundary conditions of the problem, and some remaining details, must be specified. The following boundary conditions are enforced on the cartilage specimen: (i) surface nodes which would contact the subchondral bone are coupled in all degrees of freedom (the bone is much stiffer than the cartilage), (ii) all remaining cartilage surfaces are free to deform.

As for the indenter, the geometry and material are known. A linear elastic constitutive model for an average glass is employed using $E = 75 \text{ GPa}$ and $\nu = 0.25$.²³ The position of the indenter relative to the cartilage specimen, as well as the trajectory and final indentation depth, are determined from the experimental data. Nodes on the top surface of the indenter (top circular surface in Fig. 5) are fixed to zero in all degrees of freedom.

To handle specimen interactions with both the containment vessel and the indenter, contact conditions are specified. The (discretized) cartilage is specified to remain within the cylindrical containment vessel

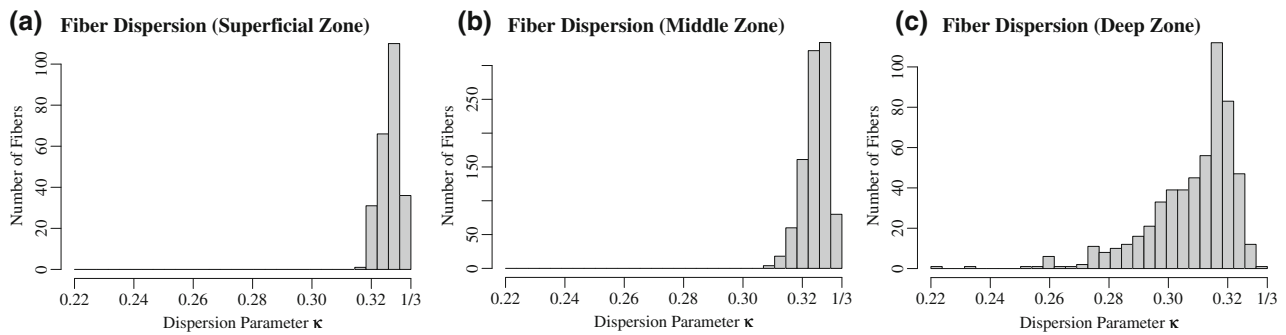


FIGURE 7. Layer-specific histograms of the structure parameter κ in the three cartilage zones, as determined directly from DTI data: (a) superficial tangential, (b) middle, (c) deep.

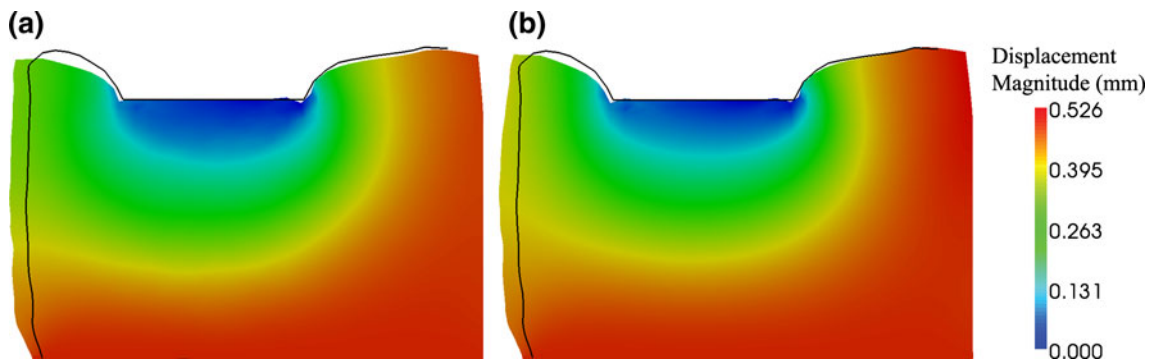


FIGURE 8. Outer boundaries of the global deformation obtained from the experiment (*solid black curves*) and the related deformations (displacement magnitude, mm) for two simulations: (a) without fiber dispersion ($\kappa \equiv 0$), and (b) with fiber dispersion ($\kappa \in [0, 1/3]$).

using a frictionless rigid-deformable contact algorithm. The contact problem between the cartilage specimen and the indenter is handled using a specialized smooth contact algorithm previously developed and documented in Kiousis *et al.*³⁸

To generate the solution, the coupled nodes on the subchondral bone surface (bottom-most surface in Fig. 5) were driven toward the indenter (along the measured trajectory), causing contact between the indenter and the upper surface of the cartilage specimen. All FE simulations were implemented in FEAP.⁵⁹

RESULTS

The global DTI deformation and the deformation of the collagen fiber fabric (both at thermodynamic equilibrium, $t \rightarrow \infty$) are compared with the simulation results using constitutive models without ($\kappa \equiv 0$) and with ($\kappa \in [0, 1/3]$) fiber dispersion.

Global Deformation

Figure 8 shows the outer boundaries of the experimentally determined global deformation (solid black

curves) with the displacement contour of the final indented FE simulations for the two material models: without considering fiber dispersion (Fig. 8a), and considering fiber dispersion (Fig. 8b). In both figures only the top and left-most experimentally determined boundaries are shown as both the bottom and right-most boundaries are constrained. The bottom is assumed straight (a good approximation which is fixed, far from the indentation location) and the right boundary is in full contact with the indenter in the undeformed configuration (evident in axial view, cf. Fig. 4c).

Deformation of the Collagen Fiber Fabric

Figure 9 provides a qualitative comparison of the deformed fiber fabric obtained from DTI data and obtained from the simulation considering fiber dispersion ($\kappa \in [0, 1/3]$): Fig. 9a illustrates the deformed fiber fabric measured from the DTI data and mapped using the deformed mesh, Fig. 9b illustrates the deformed fiber fabric determined from the simulation.

Figure 10 provides a quantitative comparison of the deformed fiber fabric obtained from DTI data and that extracted from the simulation considering fiber

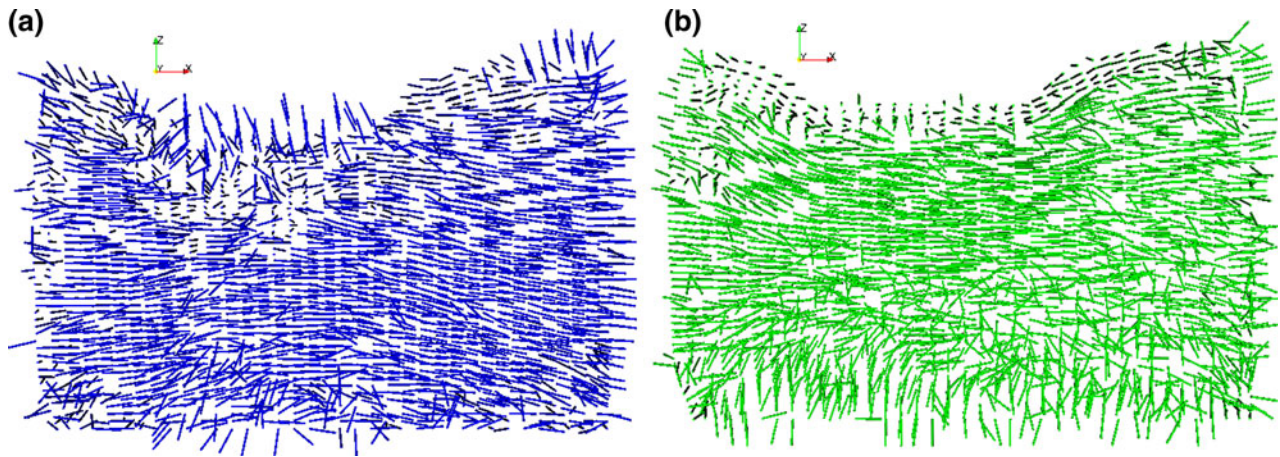


FIGURE 9. Qualitative comparison of the deformed fiber fabric obtained from DTI data and simulation considering fiber dispersion ($\kappa \in [0, 1/3]$): (a) DTI mapping using deformed simulation mesh, (b) corresponding simulation results.

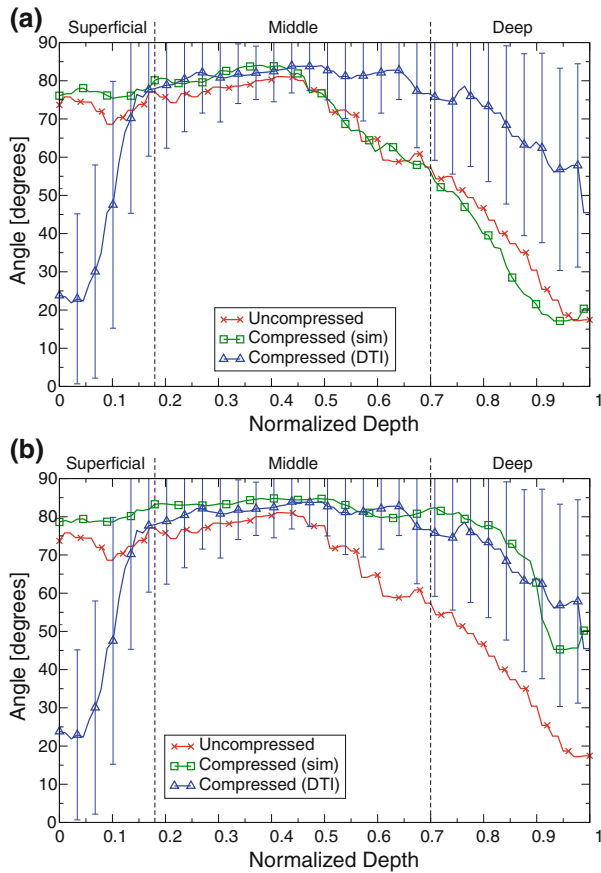


FIG. 10. Mean fiber angle (angle between fiber direction and the normal to the articular surface) vs. normalized depth from the undeformed (simulation and DT-MRI data identical) to the fully indented configuration, DT-MRI data vs. simulation with fiber dispersion ($\kappa \in [0, 1/3]$): (a) all fibers, and (b) only fibers in tension. Due to susceptibility artifacts and partial volume effects, the DT-MRI data in the deformed configuration are unreliable in the ranges ~ 0 – 0.1 and ~ 0.9 – 1.0 normalized depth.

dispersion ($\kappa \in [0, 1/3]$). To generate Figs. 10a and 10b measurements of the fiber rotations are extracted from a four-element thick region directly below the indenter. (The region of study encompasses the intersection of the DTI measurement slice and an axial projection of the indenter through the cartilage volume.) The angle is averaged in slices parallel to the cartilage surface, i.e. orthogonal to the depth direction. These averaged angles are then plotted against the normalized depth, with zero indicating the articular surface and one the interface with the subchondral bone.

The DTI data measured on the undeformed configuration is used as input for the simulation using the material model with fiber dispersion ($\kappa \in [0, 1/3]$), and thus the DTI data and the simulation have the same initial fiber fabric (shown with red \times). From this initial configuration, the final compressed fiber direction (measured in degrees and shown with green \square) is extracted from the simulation as an averaged function of depth for all fibers in the analysis region (Fig. 10a). Finally, the average compressed fiber directions extracted from the DT-MRI data are also plotted against the normalized depth (shown with blue \triangle). Figure 10b provides the same information as described above, but the simulation results are restricted to include only fibers which are in tension and thus active.

Figure 11 shows a ‘map’ of the collagen fiber stretches in the deformed configuration for the two material models: without fiber dispersion (Fig. 11a) and with fiber dispersion (Fig. 11b).

Within the layer used for the comparison (shown in Fig. 11), the fibers undergo a range of stretches in the element-wise principal fiber directions from 0.79 to 1.12 in the undispersed fiber model ($[0.68$ – $1.13]$ in the

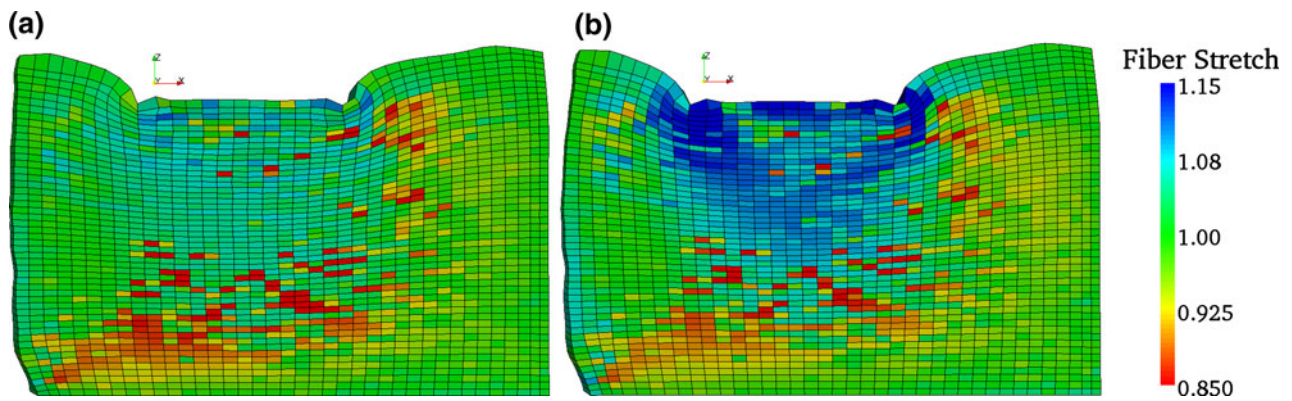


FIGURE 11. DTI voxel-matched map of the collagen fiber stretches in the fully deformed (indented) configuration for the two simulations: (a) without fiber dispersion ($\kappa=0$), and (b) with fiber dispersion ($\kappa \in [0, 1/3]$).

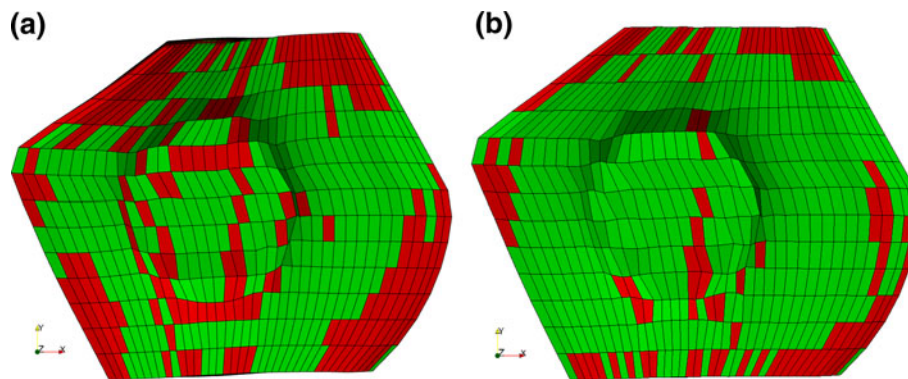


FIGURE 12. DTI voxel-matched tension (green–lighter)/compression (red–darker) map of the articular cartilage specimen in the fully deformed (indented) configuration for the two simulations: (a) without fiber dispersion ($\kappa=0$), and (b) with fiber dispersion ($\kappa \in [0, 1/3]$).

entire model) and 0.78 to 1.28 in the dispersed fiber model ([0.68–1.31] in the entire model). Figure 12 shows a corresponding ‘map’ (axial view from above, consistent with Fig. 4c) of the collagen fibers in tension (green–lighter) and compression (red–darker) for the deformed FE simulation with the two material models: without fiber dispersion (Fig. 12a) and with fiber dispersion (Fig. 12b).

DISCUSSION

Here we provide a discussion on the results, and sources of possible error in the experiments, the simulation and the comparative study. In terms of the experiments, it is important to first note that the experimental DT Image data measured in the pre- and post-indentation configurations are slightly shifted, making a direct comparison with the fully indented simulations difficult. Additionally, there is a significant change in the noise level of the post-compression DTI data, i.e. there are more artifacts due to susceptibility

alterations. Unfortunately, the artifacts are particularly bad in part of the region where the data would be most interesting—right below the indenter (particularly near the corners). Finally, there is a large anisotropy built into the measurement process (voxel resolution $50 \times 100 \mu\text{m}$ in-plane, and $800 \mu\text{m}$ of averaging out-of-plane) which leads to several problems in the evaluation. A higher out-of-plane resolution could greatly improve the results, even if the signal-to-noise ratio were to drop slightly.

Additionally, we start from a relatively poor description of the specimen geometry (one DT image slice of $800 \mu\text{m}$ thickness, and one DT image of the axial view). This could be greatly improved by using, e.g. a 3D Gradient Recalled Echo (GRE) protocol (very fast) or a 3D Turbo Spin Echo (TSE) sequence to scan the specimen geometry. The approach would lead to an excellent high resolution ($50\text{--}100 \mu\text{m}$ cubed) description of the geometry which would be perfectly aligned with the DTI data. Hence, the paper can also be viewed as a feasibility study on the methodology.

Global Deformation

The trend of the deformation response matches well despite the fact that the pre- and post-indentation DTI images (the experimental data) are slightly shifted, making a direct deformation comparison difficult. The global deformation of both the un-dispersed fiber and the dispersed fiber simulations, as shown in Fig. 8, provides a satisfactory estimate to that determined experimentally. The dispersed fiber model appears to provide a modestly better overall deformation estimate at the articular surface. The DTI data indicate that the collagen fiber fabric does have a high degree of dispersion (low fractional anisotropy), cf. Fig. 7, which is consistent with this finding.

There are several sources of potential errors. The geometry and boundary conditions may differ slightly between the experiment and simulations. The FE model is ‘flat’ due to the extrusion procedure (normal to the DTI measurement slice), while the true specimen’s interface with the underlying bone may be sloped or curved in the out-of-plane direction. Finally, the volume preserving material model will cause exaggerated lateral deformation at very large strains, although the material parameter μ is determined from the equilibrium response in the original work.⁵¹ Nonetheless, both models provide a satisfactory foundation from which to study the deformation of the fiber fabric.

Deformation of the Fiber Fabric

Several approaches are used to compare the fiber fabric deformation predicted by the simulation to that which is determined experimentally. Recall that the comparison is performed only between the original DTI data ‘slice’ and the volume equivalent part of the simulation (four element layers through the thickness), both in the final deformed configuration.

Before starting it is important to point out that a direct comparison of the first eigenvectors is sensitive to noise. Noise in DTI data will generally tend to inflate the first eigenvalue artificially and underestimate the third eigenvalue, yielding an impression of a higher anisotropy than is actually present. The degree of over-estimation is difficult to quantify.^{2,5} In addition, DTI has a low signal-to-noise ratio, especially at high resolutions. In regions with (almost) isotropic diffusivity, the eigenvalues of the estimated tensors will be roughly equal and the orientation of the eigenvectors will depend on the imaging noise. Therefore, a direct pre-/post-compression comparison of fiber orientations in such regions is inherently problematic (although this effect is somewhat mitigated if fiber dispersion is included).

To generate an empirical estimate for the change in the fiber angle, a specific method is used for mapping the post-indentation DTI data. The complex deformation in the compressed specimen immediately invalidates a direct coordinate-wise mapping of tensor positions between the pre- and post-compression measurements. Therefore, a direct validation for the fiber alignment observed in the simulation can not be achieved and we must assume a mapping of some form. The best available approximations to the unknown deformation are those estimated from the FE simulations. Since the experimental data indicate significant fiber dispersion (Fig. 8b) we use the results from the dispersed fiber model to establish this mapping. Since the deformed mesh is not aligned with the voxel grid of the post-compression DTI data, we again interpolate tensors at the element centroids using the Log-Euclidean mean.

Comparison of the deformed fiber fabric predicted from the simulations and that measured through DTI, as provided in Fig. 9, demonstrates a qualitative match in terms of the trends across the specific zones. In both simulations the fiber fabric in the superficial tangent and the middle zones becomes more aligned with the articular surface, which is consistent with the mapping of the deformed DTI data. Furthermore, some fibers in the simulated deep zone show a crimping and ‘lying down’ behavior also present in the experiment.

Qualitatively, the fiber fabric deformations measured experimentally and simulated numerically (as shown in Fig. 9) are consistent with those from de Visser *et al.*¹⁷ As discussed therein, the principal fiber orientation (for both the total averaged over all depths in the cartilage and the middle zone alone) became more aligned with the articular surface of the cartilage under compression, an effect also documented by Quinn and Morel.⁵³ However, due to the specific preparation of the specimen (the split-line is orthogonal to the DTI slice in our case), and physiological variability (we have human knee cartilage vs. bovine knee cartilage used in de Visser *et al.*¹⁷), the overall fiber orientation present in this specimen seems to be rotated in relation to the one presented in de Visser *et al.*¹⁷ The flattening effect can be observed ‘out-of-plane’, and the same is true for the alignment of the superficial layer.

The simulated fiber response is investigated more quantitatively in Fig. 10, which illustrates the change in fiber angles. Our pre-compression data matches very well with the data presented in de Visser *et al.*¹⁷ Therein, the measured fiber angles (averaged over 7 bovine knee cartilage specimens) of the principal eigenvectors in the superficial zone were $\sim 70^\circ$ (with respect to the normal to the articular surface) and in the deep zone were $\sim 20^\circ$. de Visser *et al.*¹⁷ postulate

that these values differ from the ‘ideal’ values of 90° and 0° , respectively, due to an expected degree of disorder in the orientation of the collagen fiber bundles as well as noise in the DTI data. The overall and zone-specific rotation of the simulated fiber angles for this specific specimen are consistently underestimated in relation to the corresponding mapping of the DTI data. However, we postulate that this effect is overestimated in the DTI data due to shifting of the specimen between pre- and post-measurements and the difficulty in mapping the data.

A direct comparison of the range in the change of fiber angle is also possible. de Visser *et al.*¹⁷ compress 7 bovine knee cartilage specimens on the order of $\sim 25\%$ and measure $\Delta\theta \approx 15\text{--}30^\circ$ ($\Delta\theta$ being the change in fiber angle measured as described in the section “Deformation of the Collagen Fiber Fabric”). We have one specimen of human knee cartilage compressed $\sim 20\%$ resulting in a $\Delta\theta \approx -10^\circ$ to 10° . Our result is in the range extrapolated by de Visser *et al.*¹⁷ for 20% compression, $\Delta\theta \approx 9\text{--}30^\circ$. It is important to note that de Visser *et al.*¹⁷ did measure some negative $\Delta\theta$ angles even when averaging through the full specimen thickness (all zones!). Results in the deep zone could also be effected by the afore-mentioned ‘flat’ cartilage-bone interface which may, in actuality, be curved in the out-of-plane direction.

Discussing Fig. 10 specifically, both the DT-MRI data and the simulation start from the mean fiber angles vs. normalized depth. At the articular surface the DT-MRI data are questionable in the deformed configuration because of measurement error due to the partial volume effect and the influence of the indenter material. For the same reason, the averaged DT-MRI values are also inconsistent close to the interface with underlying bone, at the bottom of the deep zone. Hence, for comparison, we should exclude the angle estimates in the ranges $\sim 0\text{--}0.1$ and $\sim 0.9\text{--}1.0$ normalized depth.

The simulated fiber angle increases under compression in the superficial and middle zones in both Figs. 10a and 10b. In the middle zone, the match between the DT-MRI data and the simulation is good. In the superficial and deep zones the simulation strays from the DT-MRI data, but at the specimen boundaries this can be attributed to the mentioned artifacts. Reviewing the deep zone specifically, when including all fibers in the comparison (Fig. 10a) the simulation results in a strange decrease in fiber angle which is inconsistent with the empirical data. If the same comparison is made with only the fibers undergoing tension (Fig. 10b), the match with the empirical data is very good, until measurement error becomes troublesome at the boundary regions. This discrepancy could be due to (i) bulging of the specimen as a result of the assumed

isochoric constitutive model, (ii) the underlying matrix material is too stiff in compression to accurately capture the change in fiber angles, or (iii) the estimated simulation geometry may be in error.

The DT-MRI data, both Figs. 10a and 10b, show an increasing standard deviation at the surface and especially in the deep zone. Crimping of the fibers could lead to greater measured ‘isotropy’ and thus greater measurement error in the first principal eigenvector. This effect could also explain the discrepancy between Figs. 10a and 10b in the deep zone. However, de Visser *et al.*¹⁶ found that the change in fractional anisotropy due to compression showed no correlation with the degree of compression.

Despite these drawbacks the range of simulation predicted fiber rotations matches well with the ranges determined experimentally by de Visser *et al.*¹⁷ Therein, the authors measured total mean fiber rotations at $\sim 20\%$ compression in a range from $\sim 9^\circ$ to $\sim 30^\circ$, with a mean trend-line at $\sim 20^\circ$. Without fiber dispersion the simulated fiber angles change by up to approximately 22° in the middle zone, while the fiber angles change up to approximately 26° in the model considering fiber dispersion.

The simulations are also able to predict which fibers are in tension or compression, and furthermore, by how much (Fig. 11). Therein, the collagen fiber stretches in the deformed configuration are shown (in the voxel-wise principal fiber directions) for the two material models: without fiber dispersion (Fig. 11a), and with fiber dispersion (Fig. 11b). As can be clearly seen, the dispersed fiber model distributes the load to put the fibers under greater tension, especially directly under the indenter. This effect is also evident in the increased fiber stretch ranges determined from the simulation including fiber dispersion ($[0.79\text{--}1.12]$ in the undispersed fiber model vs. $[0.78\text{--}1.28]$ in the dispersed model).

The unique cartilage material exhibits an interesting response during unconfined indentation loading. The superficial tangent layer is, for all practical purposes, loaded in a manner that puts the collagen fibers in tension (although this effect is less pronounced in the model without fiber dispersion). This effect has been postulated and noted by several authors, see, e.g. Glaser and Putz,²⁴ Wilson *et al.*⁶⁵ and Quinn and Morel.⁵³ The cartilage volume in the middle and deep zones distributes the load in a remarkable way such that a large portion of the fibers support a tensile load even directly below the indenter. The tension-compression response of collagen fibers is crucial to the overall mechanical response of articular cartilage. These results are also consistent with SEM findings from Glaser and Putz,²⁴ demonstrating a fiber alignment in

bovine hip cartilage consistent with predominantly tensile stress (even directly underneath an indenter).

Finally, to focus more on the significant differences between the undispersed and dispersed fiber models, the axial view from above is used to generate a tension-compression ‘map’ for the fibers, as shown in Fig. 12. There is a clear difference in the tension-compression maps from the model without fiber dispersion (Fig. 12a) to the model with fiber dispersion (Fig. 12b). Overall, the dispersed fiber model appears to be more consistent with the literature in that the superficial layer is almost completely in tension.

Limitations and Potential Applications

Several authors have proposed multi-phasic constitutive models (see, e.g. Li *et al.*,⁴¹ DiSilvestro and Suh,¹⁸ Li and Herzog,⁴⁰ Wilson *et al.*,⁶⁴ Quinn and Morel,⁵³ García and Cortés²¹ and Julkunen *et al.*³³), which describe much of the important structural phenomena. These studies have shed significant light on the structure–function relationships of the various cartilage constituents, but frequently these models are limited to one- or two-dimensional analytical solutions or simulations, and thus can be difficult to generalize to 3D patient-specific simulations.

The proposed FE modeling approach uses a small number of material parameters all of which are structurally-motivated and have a direct physical interpretation. The approach is efficient enough to enable large scale 3D simulations of cartilage deformation and contact. To make the methods more tractable for large scale patient-specific modeling, an implementation proposed by Taylor *et al.*⁶⁰ could be employed. In this approach the authors introduce an efficient constitutive update scheme for anisotropic viscoelastic models and present a graphics processing unit (GPU) implementation for FE modeling. In FE test cases against a traditional central processing unit the GPU implementation resulted in an $8 \times$ to $56 \times$ decrease in solution time depending on the number of degrees of freedom in the model.

The modeling framework proposed herein also incorporates the principal direction of the collagen fibers and a measure of fiber dispersion (experimentally determined) as a finite element input allowing the deformation of a specimen- or patient-specific fiber fabric to be tracked under finite deformation. Numerical simulation of cartilage incorporating DT-MRI has potential applications in evaluating the cartilage matrix integrity since DT-MRI is sensitive to both the proteoglycan content (through the Apparent Diffusion Coefficient (ADC)⁴⁴) and the collagen network (through the FA and the first Eigenvector). Changes in the ADC have been observed

in proteoglycan depleted cartilage,⁴⁴ whereas both FA and 1st Eigenvector remained unchanged. Analysis of the changes in DTI parameters under loading conditions may reveal important information about the integrity of human articular cartilage, since degeneration in the early phases of osteoarthritis is known to alter the mechanical properties.

It should be noted that contrary to the T2 relaxation time, another MRI parameter which is sensitive to the collagen matrix, DTI is not affected by the magic angle effect, since all images are acquired with the same T2-weighting (i.e. with the same TE and TR). Indeed, one possible application of DTI is to quantify the effect of the magic angle in T2 relaxation time *in vivo*, since changes in T2 due to reorientation of the 1st Eigenvector could be performed.

MRI alone can not yet be used to determine the functional state of articular cartilage.^{11,15,32,52,70} There is hope that a multi-disciplinary combination of DT-MR Imaging and numerical simulation will bring this goal to fruition, as discussed in, e.g. the recent paper by Xia.⁷⁰

ACKNOWLEDGMENTS

We gratefully acknowledge the financial support of the Austrian Science Fund through project P-18110-B15 ‘Visualization of biomechanics of articular cartilage by MRI’. In addition, we acknowledge Dimitris Kiousis for several lengthy discussions and support regarding the use of a custom smooth contact algorithm, as well as general support regarding FEAP.

REFERENCES

- ¹Abdullah, O. M., S. F. Othman, X. J. Zhou, and R. L. Magin. Diffusion tensor imaging as an early marker for osteoarthritis. *Proc. Intl. Soc. Magn. Reson. Med.* 15:814, 2007.
- ²Alexander, A. L., K. Hasan, G. Kindlmann, D. L. Parker, and J. S. Tsuruda. A geometric analysis of diffusion tensor measurements of the human brain. *Magn. Reson. Med.* 44:283–291, 2000.
- ³Arsigny, V., P. Fillard, X. Pennec, and N. Ayache. Geometric means in a novel vector space structure on symmetric positive-definite matrices. *SIAM J. Matrix Anal. Appl.* 29:328–347, 2006.
- ⁴Bachrach, N. M., V. C. Mow, and F. Guilak. Incompressibility of the solid matrix of articular cartilage under high hydrostatic pressures. *J. Biomech.* 31:445–451, 1998.
- ⁵Bastin, M. E., P. A. Armitage, and I. Marshall. A theoretical study of the effect of experimental noise on the measurement of anisotropy in diffusion imaging. *Magn. Reson. Imaging* 16(7):773–785, 1998.
- ⁶Benninghoff, A. Form und Bau der Gelenkknorpel in ihren Beziehungen zur Funktion. II. Der Aufbau des

- Gelenknorpels in seinen Beziehungen zur Funktion. *Zeitschrift für Zellforschung und mikroskopische Anatomie* 2:783–862, 1925.
- ⁷Bodammer, N., J. Kaufmann, M. Kanowski, and C. Tempelman. Eddy current correction in diffusion-weighted imaging using pairs of images acquired with opposite diffusion gradient polarity. *Magn. Reson. Med.* 51:188–193, 2004.
- ⁸Boskey, A., and N. P. Camacho. FT-IR imaging of native and tissue-engineered bone and cartilage. *Biomaterials* 28:2465–2478, 2007.
- ⁹Broom, N. D. Further insights into the structural principles governing the function of articular cartilage. *J. Anat.* 139:275–294, 1984.
- ¹⁰Broom, N. D., and R. Flachsmann. Physical indicators of cartilage health: the relevance of compliance, thickness, swelling and fibrillar texture. *J. Anat.* 202:481–494, 2003.
- ¹¹Burstein, D., and M. L. Gray. Is MRI fulfilling its promise for molecular imaging of cartilage in arthritis? *Osteoarthr. Cartil.* 14:1087–1090, 2006.
- ¹²Charlebois, M., M. D. McKee, and M. D. Buschmann. Nonlinear tensile properties of bovine articular cartilage and their variation with age and depth. *J. Biomech. Eng.* 126:129–137, 2004.
- ¹³Clark, J. M. The organization of collagen fibrils in the superficial zones of articular cartilage. *J. Anat.* 171:117–130, 1990.
- ¹⁴Demiray, H. A note on the elasticity of soft biological tissues. *J. Biomech.* 5:309–311, 1972.
- ¹⁵Deng, X., M. Farley, M. T. Nieminen, M. Gray, and D. Burstein. Diffusion tensor imaging of native and degenerated human articular cartilage. *Magn. Reson. Med.* 25(2):168–171, 2007.
- ¹⁶de Visser, S. K., J. C. Bowden, E. Wentrup-Bryne, L. Rintoul, T. Bostrom, J. M. Pope, and K. I. Momot. Anisotropy of collagen fibre alignment in bovine cartilage: comparison of polarised light microscopy and spatially resolved diffusion-tensor measurements. *Osteoarthr. Cartil.* 16:689–697, 2008.
- ¹⁷de Visser, S. K., R. W. Crawford, and J. M. Pope. Structural adaptations in compressed articular cartilage measured by diffusion tensor imaging. *Osteoarthr. Cartil.* 16:83–89, 2008.
- ¹⁸DiSilvestro, M. R., and J.-K. F. Suh. A cross-validation of the biphasic poroviscoelastic model of articular cartilage in unconfined compression, indentation, and confined compression. *J. Biomech.* 34:519–525, 2001.
- ¹⁹Ennis, D. B., G. Kindlman, I. Rodriguez, P. A. Helm, and E. R. McVeigh. Visualization of tensor fields using superquadric glyphs. *Magn. Reson. Med.* 53:169–176, 2005.
- ²⁰Filidoro, L., O. Dietrich, J. Weber, E. Rauch, T. Oether, M. Wick, M. F. Reiser, and C. Glaser. High-resolution diffusion tensor imaging of human patellar cartilage: feasibility and preliminary findings. *Magn. Reson. Med.* 53:993–998, 2005.
- ²¹García, J. J., and D. H. Cortés. A biphasic viscohyperelastic fibril-reinforced model for articular cartilage: formulation and comparison with experimental data. *J. Biomech.* 40:1737–1744, 2007.
- ²²Gasser, T. C., R. W. Ogden, and G. A. Holzapfel. Hyperelastic modelling of arterial layers with distributed collagen fibre orientations. *J. R. Soc. Interface* 3:15–35, 2006.
- ²³Gere, J. M., and S. P. Timoshenko. *Mechanics of Materials*, 4th edn. Boston, MA: PWS-KENT Pub. Co., 1997.
- ²⁴Glaser, C., and R. Putz. Functional anatomy of articular cartilage under compressive loading quantitative aspects of global, local and zonal reactions of the collagenous network with respect to the surface integrity. *Osteoarthr. Cartil.* 10:83–99, 2002.
- ²⁵Hayes, W. C., and A. J. Bodine. Flow-independent viscoelastic properties of articular cartilage matrix. *J. Biomech.* 11:407–419, 1978.
- ²⁶Holzapfel, G. A. *Nonlinear Solid Mechanics. A Continuum Approach for Engineering*. Chichester: Wiley, 2000.
- ²⁷Holzapfel, G. A., and T. C. Gasser. A viscoelastic model for fiber-reinforced composites at finite strains: Continuum basis, computational aspects and applications. *Comput. Meth. Appl. Mech. Eng.* 190:4379–4403, 2001.
- ²⁸Holzapfel, G. A., T. C. Gasser, and R. W. Ogden. A new constitutive framework for arterial wall mechanics and a comparative study of material models. *J. Elasticity* 61:1–48, 2000.
- ²⁹Holzapfel, G. A., T. C. Gasser, and R. W. Ogden. Comparison of a multi-layer structural model for arterial walls with a Fung-type model, and issues of material stability. *J. Biomech. Eng.* 126:264–275, 2004.
- ³⁰Huang, C.-Y., A. Stankiewicz, G. A. Ateshian, and V. C. Mow. Anisotropy, inhomogeneity, and tension-compression nonlinearity of human glenohumeral cartilage in finite deformation. *J. Biomech.* 38:799–809, 2005.
- ³¹Jeffery, A. K., G. W. Blunn, C. W. Archer, and G. Bentley. Three-dimensional collagen architecture in bovine articular cartilage. *J. Bone Joint Surg. Br.* 73:795–801, 1991.
- ³²Julkunen, P., P. Kiviranta, W. Wilson, J. S. Jurvelin, and R. K. Korhonen. Characterization of articular cartilage by combining microscopic analysis with a fibril-reinforced finite-element model. *J. Biomech.* 40:1862–1870, 2007.
- ³³Julkunen, P., R. K. Korhonen, W. Herzog, and J. S. Jurvelin. Uncertainties in indentation testing of articular cartilage: a fibril-reinforced poroviscoelastic study. *Med. Eng. Phys.* 30:506–515, 2008.
- ³⁴Jurvelin, J. S., M. D. Buschmann, and E. B. Hunziker. Optical and mechanical determination of Poisson's ratio of adult bovine humeral articular cartilage. *J. Biomech.* 30:235–241, 1997.
- ³⁵Kaab, M. J., I. A. Gwynn, and H. P. Notzli. Collagen fibre arrangement in the tibial plateau articular cartilage of man and other mammalian species. *J. Anat.* 193:23–34, 1998.
- ³⁶Kaab, M. J., K. Ito, J. M. Clark, and H. P. Notzli. Deformation of articular cartilage collagen structure under static and cyclic loading. *J. Orthop. Res.* 16:743–751, 1998.
- ³⁷Kaab, M. J., K. Ito, B. Rahn, J. M. Clark, and H. P. Notzli. Effect of mechanical load on articular cartilage collagen structure: a scanning electron-microscope study. *J. Anat.* 167:106–120, 2000.
- ³⁸Kiouis, D. E., T. C. Gasser, and G. A. Holzapfel. Smooth contact strategies with emphasis on the modeling of balloon angioplasty with stenting. *Int. J. Numer. Meth. Eng.* 75:826–855, 2008.
- ³⁹Le Bihan, D., J.-F. Mangin, C. Poupon, C. A. Clark, S. Pappata, N. Molko, and H. Chabriat. Diffusion tensor imaging: concepts and applications. *J. Musculoskel. Neuron. Interact.* 13:534–546, 2001.
- ⁴⁰Li, L. P., and W. Herzog. The role of viscoelasticity of collagen fibers in articular cartilage: theory and numerical formulation. *Biorheology* 41:181–194, 2004.
- ⁴¹Li, L. P., J. Soulhat, M. D. Buschmann, and A. Shirazi-Adl. Nonlinear analysis of cartilage in unconfined ramp

- compression using a fibril reinforced poroelastic model. *Clin. Biomech.* 14:673–682, 1999.
- ⁴²Marr, D., and E. Hildreth. Theory of edge detection. *Proc. R. Soc. Lond. B* 207:187–217, 1980.
- ⁴³Mattiello, J., J. P. Basser, and D. Le Bihan. The b matrix in diffusion tensor echo-planar imaging. *Magn. Reson. Med.* 37:292–300, 1997.
- ⁴⁴Meder, R., S. K. de Visser, J. C. Bowden, T. Bostrom, and J. M. Pope. Diffusion tensor imaging of articular cartilage as a measure of tissue microstructure. *Osteoarthr. Cartil.* 14:875–881, 2006.
- ⁴⁵Moger, C. J., R. Barrett, P. Bleuett, D. A. Bradley, R. E. Ellis, E. M. Green, K. M. Knapp, P. Muthuvelu, and C. P. Winlove. Regional variations of collagen orientation in normal and diseased articular cartilage and subchondral bone determined using small angle X-ray scattering (SAXS). *Osteoarthr. Cartil.* 15:682–687, 2007.
- ⁴⁶Mollenhauer, J., M. Aurich, C. Muehleman, G. Khelashvili, and T. C. Irvine. X-ray diffraction of the molecular substructure of human articular cartilage. *Connect. Tissue Res.* 44:201–207, 2003.
- ⁴⁷Mow, V. C., W. Y. Gu, and F. H. Chen. Structure and function of articular cartilage and meniscus. In: *Basic Orthopaedic Biomechanics & Mechano-Biology*, 3rd edn., edited by V. C. Mow and R. Huiskes. Philadelphia: Lippincott Williams & Wilkins, 2005, pp. 181–258.
- ⁴⁸Muehleman, C., S. Majumdar, A. S. Issever, F. A. R.-H. Menk, L. Rigon, G. Heitner, B. Reime, J. Metge, A. Wagner, K. E. Kuettner, and J. Mollenhauer. X-ray detection of structural orientation in human articular cartilage. *Osteoarthr. Cartil.* 12:97–105, 2004.
- ⁴⁹Neeman, M., J. P. Freyer, and L. O. Sillerud. A simple method for obtaining cross-term-free images for diffusion anisotropy studies in NMR microimaging. *Magn. Reson. Med.* 21:138–143, 1991.
- ⁵⁰Park, S., R. Krishnan, S. B. Nicoll, and G. A. Ateshian. Cartilage interstitial fluid load support in unconfined compression. *J. Biomech.* 36:1785–1796, 2003.
- ⁵¹Pierce, D. M., W. Trobin, S. Trattng, H. Bischof, and G. A. Holzapfel. A phenomenological approach toward patient-specific computational modeling of articular cartilage including collagen fiber tracking. *J. Biomed. Eng.* 131:091006, 2009.
- ⁵²Potter, H. G., B. R. Black, and L. R. Chong. New techniques in articular cartilage imaging. *Clin. Sports Med.* 28:77–94, 2009.
- ⁵³Quinn, T. M., and V. Morel. Microstructural modeling of collagen network mechanics and interactions with the proteoglycan gel in articular cartilage. *Biomech. Model. Mechanobiol.* 6:73–82, 2007.
- ⁵⁴Roth, V., and V. C. Mow. The intrinsic tensile behavior of the matrix of bovine articular cartilage and its variation with age. *J. Bone Joint Surg.* 62:1102–1117, 1980.
- ⁵⁵Schmidt, M. B., V. C. Mow, L. E. Chun, and D. R. Eyre. Effects of proteoglycan extraction on the tensile behavior of articular cartilage. *J. Orthop. Res.* 8:353–363, 1990.
- ⁵⁶Silver, F. H., G. Bradica, and A. Tria. Viscoelastic behavior of osteoarthritic cartilage. *Connect. Tissue Res.* 42:223–233, 2001.
- ⁵⁷Simo, J. C. On a fully three-dimensional finite-strain viscoelastic damage model: formulation and computational aspects. *Comput. Meth. Appl. Mech. Eng.* 60:153–173, 1987.
- ⁵⁸Simo, J. C., R. L. Taylor, and K. S. Pister. Variational and projection methods for the volume constraint in finite deformation elasto-plasticity. *Comput. Meth. Appl. Mech. Eng.* 51:177–208, 1985.
- ⁵⁹Taylor, R. L. FEAP—A Finite Element Analysis Program, Version 8.2 User Manual. University of California at Berkeley, Berkeley, California, 2007.
- ⁶⁰Taylor, Z. A., O. Comas, M. Cheng, J. Passenger, D. J. Hawkes, D. Atkinson, and S. Ourselin. On modelling of anisotropic viscoelasticity for soft tissue simulation: numerical solution and GPU execution. *Med. Image Anal.* 13:234–244, 2009.
- ⁶¹Ugryumova, N., D. P. Attenburrow, C. P. Winlove, and S. J. Matcher. The collagen structure of equine articular cartilage, characterized using polarization-sensitive optical coherence tomography. *J. Phys. D: Appl. Phys.* 38:2612–2619, 2005.
- ⁶²Ugryumova, N., S. V. Gangnus, and S. J. Matcher. Three-dimensional optic axis determination using variable-incidence-angle polarization-optical coherence tomography. *Opt. Lett.* 31:2305–2307, 2006.
- ⁶³Wilson, W., J. M. Huyghe, and C. C. van Donkelaar. A composition-based cartilage model for the assessment of compositional changes during cartilage damage and adaptation. *Osteoarthr. Cartil.* 14:554–560, 2006.
- ⁶⁴Wilson, W., J. M. Huyghe, and C. C. van Donkelaar. Depth-dependent compressive equilibrium properties of articular cartilage explained by its composition. *Biomech. Model. Mechanobiol.* 43–53, 2007.
- ⁶⁵Wilson, W., C. C. van Donkelaar, B. van Rietbergen, K. Ito, and R. Huiskes. Stresses in the local collagen network of articular cartilage: a poroviscoelastic fibril-reinforced finite element study. *J. Biomech.* 37:357–366, 2004.
- ⁶⁶Wilson, W., C. C. van Donkelaar, B. van Rietbergen, and R. Huiskes. A fibril-reinforced poroviscoelastic swelling model for articular cartilage. *J. Biomech.* 38:1195–1204, 2005.
- ⁶⁷Witkin, A. P. Scale-space filtering. In: *Proceedings of the International Joint Conference on Artificial Intelligence*, 1983, pp. 1019–1022.
- ⁶⁸Wong, M., M. Ponticello, V. Kovanen, and J. S. Jurvelin. Volumetric changes of articular cartilage during stress relaxation in unconfined compression. *J. Biomech.* 33:1049–1054, 2000.
- ⁶⁹Woo, S. L. Y., B. R. Simon, S. C. Kuei, and W. H. Akeson. Quasi-linear viscoelastic properties of normal articular cartilage. *J. Biomech. Eng.* 102:85–90, 1980.
- ⁷⁰Xia, Y. Resolution ‘scaling law’ in MRI of articular cartilage. *Osteoarthr. Cartil.* 15:363–365, 2007.
- ⁷¹Xia, Y., J. B. Moody, and H. Alhadlaq. Orientational dependence of T2 relaxation in articular cartilage: a microscopic MRI (microMRI) study. *Magn. Reson. Med.* 48:460–469, 2002.
- ⁷²Zhu, W., V. C. Mow, T. J. Koob, and D. R. Eyre. Viscoelastic shear properties of articular cartilage and the effects of glycosidase treatments. *J. Orthop. Res.* 11:771–781, 1993.